Nanoscale

PAPER

Cite this: *Nanoscale*, 2017, **9**, 4445

Bacterial cellulose-based sheet-like carbon aerogels for the *in situ* growth of nickel sulfide as high performance electrode materials for asymmetric supercapacitors†

Lizeng Zuo,[a] Wei Fan,*[b] Youfang Zhang,[a] Yunpeng Huang,[a] Wei Gao[a] and Tianxi Liu*[a,b]

Electroactive materials, such as nickel sulfide (NiS), with high theoretical capacities have attracted broad interest to fabricate highly efficient supercapacitors. Preventing aggregation and increasing the conductivity of NiS particles are key challenging tasks to fully achieve excellent electrochemical properties of NiS. One effective approach to solve these problems is to combine NiS with highly porous and conductive carbon materials such as carbon aerogels. In this study, a green and facile method for the *in situ* growth of NiS particles on bacterial cellulose (BC)-derived sheet-like carbon aerogels (CAs) has been reported. CA prepared by the dissolution–gelation–carbonization process was used as a framework to construct NiS/CA composite aerogels with NiS uniformly decorated on the pore walls of CA. It was found that the NiS/CA composite aerogel electrodes exhibit excellent capacitive performance with high specific capacitance (1606 F g^{-1}), good rate capacitance retention (69% at 10 A g^{-1}), and enhanced cycling stability (91.2% retention after 10 000 continuous cyclic voltammetry cycles at 100 mV s^{-1}). Furthermore, asymmetric supercapacitors (ASCs) were constructed utilizing NiS/CA composite and CA as the positive and negative electrode materials, respectively. Through the synergistic effect of three-dimensional porous structures and conductive networks derived from CA and the high capacitive performance offered by NiS, the ASC device exhibited an energy density of ~21.5 Wh kg^{-1} and a power density of 700 W kg^{-1} at the working voltage of 1.4 V in 2 M KOH aqueous solution. The ASC device also showed excellent long-term cycle stability with ~87.1% specific capacitance retention after 10 000 cycles of cyclic voltammetry scans. Therefore, the NiS/CA composite shows great potential as a promising alternative to high-performance electrode materials for supercapacitors.

Received 6th January 2017,
Accepted 3rd March 2017

DOI: 10.1039/c7nr00130d

rsc.li/nanoscale

Introduction

It is in great demand to develop efficient and sustainable energy conversion and storage devices due to gradual depletion of fossil fuels and increasing severity of environmental issues. Supercapacitors, one of the most promising electrical energy-storage devices, also known as electrochemical capacitors, have attracted significant attention because of their high power density, long cycle stability, fast charge–discharge rates, and low maintenance cost.[1–3] Supercapacitors, according to the energy storage mechanisms, can be divided into electrical double layer (EDL) capacitors and pseudocapacitors.[4] Compared with EDL capacitors, pseudocapacitors hold much higher specific capacitance and energy density due to the fast and reversible faradaic processes correlating with electroactive species.[5]

Regarding advanced electroactive materials applied in supercapacitors, transition metal oxides or hydroxides,[6–9] conducting polymers,[10–13] and materials possessing oxygen- and nitrogen-containing functional groups on their surface[5] are considered as the most promising materials for exploring a new generation of supercapacitors. Recently, various metal sulfides including $NiCo_2S_4$,[14–16] Ni_3S_2,[17] CuS,[18] SnS_2,[19] CoS_2,[20] and CoS_{12} [21] with nanostructures have been widely explored as a new type of electroactive materials for pseudocapacitors due to their relatively high theoretical capacitance and excellent redox reversibility compared with those of their oxide

[a]State Key Laboratory of Molecular Engineering of Polymers, Department of Macromolecular Science, Fudan University, Shanghai, 200433, P. R. China. E-mail: txliu@fudan.edu.cn, txliu@dhu.edu.cn
[b]State Key Laboratory of Modification of Chemical Fibers and Polymer Materials, College of Materials Science and Engineering, Donghua University, 2999 North Renmin Road, Shanghai 201620, P. R. China. E-mail: weifan@dhu.edu.cn

†Electronic supplementary information (ESI) available: Table S1 and Fig. S1–S13. See DOI: 10.1039/c7nr00130d

counterparts. As one of these metal sulfides, nickel sulfide (NiS) has attracted significant interest due to its relatively high theoretical capacity, cost-effectiveness, easy fabrication process, and environmental sustainability.[22,23] However, further practical applications of NiS as electroactive materials for pseudocapacitors are still restricted by the low power density resulting from the poor electrical conductivity, limited electron transport rate, as well as shortage of cycling stability due to easy deformation during the redox process.[24] Therefore, one effective method to resolve the abovementioned problems is to use carbon-based materials with high electrical conductivity and high specific surface area as the backbone materials to hybridize with electroactive NiS.

Considering the unique physical properties such as high electrical conductivity, porosity, and large specific surface area of carbon aerogels, they are regarded as one of the most suitable supporting materials for the fabrication of pseudocapacitor electrodes.[25] Based on the carbon resource, carbon aerogels, composed of interconnected three-dimensional (3D) networks, can be divided into three categories: carbon-based (graphene, carbon nanotubes (CNTs), graphene nanoribbon, *etc.*),[26–28] synthetic organic polymer-based (resorcinol-formaldehyde, phenolic-furfural, *etc.*),[29] and natural polymer or biomass-based (cellulose, winter melon, *etc.*) carbon aerogels.[30–32] Although CNTs and graphene can be used as building blocks to construct macroscopic 3D architectures, the costly raw materials and complex synthetic processes are the main obstacles for these new types of carbon aerogels to be accepted in commercial applications.[33,34] In addition, carbon aerogels carbonized from synthetic organic polymer highly rely on the utilization of harmful chemicals such as formaldehyde and furfural, which have been restricted by environmental regulations.[35,36] Therefore, exploring a facile, environmentally friendly, and cost-effective preparation process for carbon aerogels is highly desirable. To this end, biomass based-carbon aerogels, possessing low-cost, small environmental footprint, and easy fabrication, represent a new research direction in carbon aerogels. Bacterial cellulose (BC), a typical biomass material, can be produced in large-scale *via* a microbial fermentation process. BC composed of interconnected networks of cellulose nanofibers has attracted significant attention due to its wide availability, low-cost, renewability, and porous nature.[37,38] Furthermore, BC pellicles have been employed to fabricate macroscopic-scale carbon nanofiber aerogels, which are characterized by high electrical conductivity, porosity, and specific surface area, exhibiting excellent potential applications as electrode materials. For instance, Long *et al.* used BC as both template and precursor for the synthesis of a nitrogen-doped carbon network through the direct carbonization of polyaniline-coated BC.[39] The obtained carbon networks can act not only as a support for obtaining high capacitance electrode materials, but also as conductive networks to integrate active electrode materials. Li *et al.* reported freestanding and flexible supercapacitor electrodes fabricated using BC, CNTs, and polyaniline *via* mixing the pulped BC and CNT suspension followed by vacuum filtration and an electrodeposition process.[40] Lai *et al.* fabricated nitrogen-doped carbon nanofiber composites derived from BC pellicles for use as cost-effective electrocatalysts.[41] However, direct carbonization or vacuum filtration of cellulose pellicles results in carbon aerogels that are composed of nanofibers with diameter of several nanometers, which is difficult for further growth of nanoparticles to larger sizes. Therefore, tuning the structure of BC-derived carbon aerogels is of great importance for the further growth of electroactive materials.

In this study, BC-derived carbon aerogels (CAs) were prepared by the dissolution–gelation–carbonization approach, which is a new strategy to fabricate 3D porous carbon materials derived from low-cost cellulose-based materials. The resulting carbon materials comprised a sheet-like structure instead of nanofibers, which can offer more anchoring sites for electroactive particles with larger size and provide much higher electrical conductivity for accelerating the electron transfer. NiS nanoparticles, one type of faradaic capacitive electrode materials, were grown on the pore walls of CA *via* a simple hydrothermal route. Through synergistic effect of 3D porous structures and conductive networks derived from CA and the high capacitive performance offered by NiS, the obtained NiS/CA composite aerogels exhibited excellent electrochemical performance with high specific capacitance and good capacitive retention after 10 000 cycles. Moreover, the asymmetric supercapacitor, with NiS/CA composite and CA as the positive and negative electrode materials, respectively, exhibited a wide working voltage window of 0–1.4 V and a high energy density of ~21.5 Wh kg^{-1} at the power density of 700 W kg^{-1}, as well as excellent cycle lifetime (~87.1%) after 10 000 cycles of cyclic voltammetry scans, demonstrating its great potential as a promising candidate for high-performance supercapacitors.

Experimental

Materials

The BC pellicles were supplied by Hainan Yide Food Co. Ltd. Thiourea was purchased from Aladdin Chemical Reagent Co. Nickel nitrate hexahydrate ($Ni(NO_3)_2{\cdot}6H_2O$), sodium hydroxide (NaOH), urea, and *N*,*N*-dimethylformamide (DMF) were obtained from Sinopharm Chemical Reagent Co. Ltd. All the reagents were used as received without further purification. Deionized (DI) water was used as a solvent throughout the experiments.

Preparation of the BC-derived carbon aerogels (CAs)

The as-received BC pellicles were soaked in 0.1 M NaOH aqueous solution for 6 h to remove the impurities and then rinsed with DI water several times until neutral. Subsequently, the purified BC pellicles were frozen in liquid nitrogen (−196 °C), and dried in a freeze-dryer (VFD-1000, Beijing BO Kang Experimental Medical Instrument Co.) for ice sublimation. The dried BC pellicles were immersed in 7% NaOH/12% urea aqueous solutions to form a mixture in which the BC

content was 2.5 wt% and pre-cooled to −12 °C in a refrigerator. Then, the resulting mixture was stirred at 2000 rpm for 20 min to form a homogeneous BC slurry. Then, the as-prepared dispersion was transferred to a tubular mould and heated at 80 °C for 5 h to form a gel before extraction in DI water. After 24 h, the cylindrical BC hydrogels were frozen in liquid nitrogen and subsequently freeze-dried for 48 h to form BC aerogels. Finally, CAs were obtained by carbonization of the BC aerogels under flowing nitrogen at 800 °C for 2 h with a heating rate of 5 °C min^{-1}.

Preparation of the NiS/CA composite aerogels

NiS/CA composite aerogels with different mass loading of NiS were synthesized by a solvothermal reaction process. In detail, a desired amount of $Ni(NO_3)_2$ (2, 4, and 6 mmol) and thiourea with the molar ratio of 1 : 2 was dissolved in 30 mL mixed solution of DI water/DMF with the volume ratio of 1 : 2. After this, CA was immersed in the abovementioned composite solution and left to stand for 1 h. Subsequently, the mixture was transferred to a Teflon stainless-steel autoclave, solvothermally reacted at 180 °C for 12 h, and naturally cooled down to room temperature. Then, the resulting products were rinsed with DI water several times and dried at 70 °C. The hybrids with different loading amounts of NiS were denoted as NiS/CA-1, NiS/CA-2, and NiS/CA-3. For comparison, pure NiS was also synthesized using the same procedure without the addition of CA. The overall preparation process of NiS/CA composites is shown in Fig. 1.

Characterization

Transmission electron microscopy (TEM) images of the obtained CA samples were acquired using a Tecnai G2 20 TWIN TEM (FEI, America) at the accelerating voltage of 200 kV. Before carrying out TEM study, the CA samples were ground to a powder and dispersed in a certain amount of water and ultrasonicated for 0.5 h. Then, the dispersion of CA was dropped onto copper mesh for drying. Field emission scanning electron microscopy (FESEM) (Ultra 55, Zeiss) was used to characterize the morphologies of the samples under the acceleration voltage of 5 kV. The specific surface area of the samples were investigated using a ASIQMU00U00-6 surface area detecting instrument (Quanachrome, America) by the Brunauer–Emmett–Teller (BET) method. The pore size distribution was obtained from the adsorption branches of isotherms by the Barrett–Joyner–Halenda (BJH) method. The electrical conductivity of the bulk samples was measured by a RTS-8 four-probe electric measuring instrument (Four Probes Tech., China). The crystalline structures of the obtained samples were acquired by X-ray diffraction (XRD) (X'pert PRO, PANalytical) with Cu K_α radiation (λ = 0.1542 nm) under a voltage of 40 kV and a current of 40 mA with 2θ ranging from 10° to 80°. The chemical composition of the obtained samples was investigated *via* X-ray photoelectron spectroscopy (XPS) using a PHI-5000C ESCA device (PerkinElmer) and the spectra were corrected with C 1s at 284.5 eV. The curve fitting and background subtraction were accomplished using XPS PEAK41 software. Raman spectra were obtained *via* a Horiba Laser Raman Spectrometer (Horiba JobinYvon, France) operating at 532 nm.

Electrochemical measurements with a three-electrode system

The NiS/CA electrodes were fabricated based on a previously reported procedure.[25] Briefly, NiS/CA was ground into powder and then NiS/CA powder, acetylene black, polytetrafluoroethylene (PTFE) emulsion (60 wt% PTFE in H_2O) were mixed at the mass ratio of 80 : 10 : 10 and wetted by ethanol to obtain a homogeneous slurry. Then, the obtained slurry was rolled into a thin film and further dried at 70 °C for 12 h. Finally, the NiS/CA composite electrodes were prepared with nickel-foam as the current collector. After this, the electrochemical measurements were performed in 2 M KOH aqueous solution at room

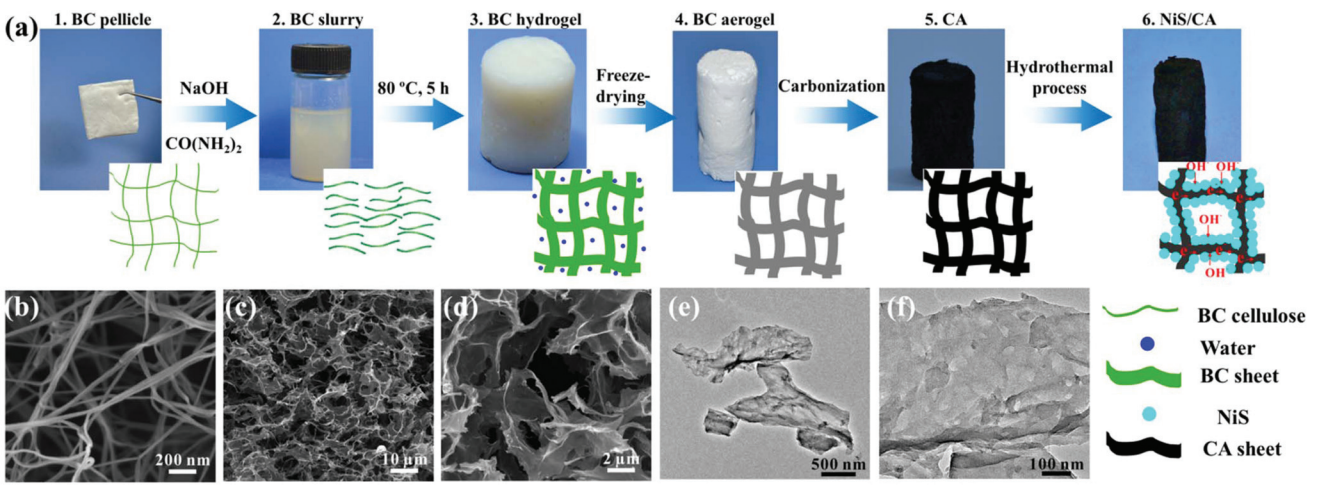

Fig. 1 Preparation and morphologies of the NiS/CA aerogels. (a) Schematic of the preparation process. (1) Freeze-dried BC pellicle. (2) BC slurry. (3) BC hydrogel from the regenerated slurry. (4) BC aerogel. (5) CA aerogel. (6) NiS/CA aerogel. (b) SEM image of the BC pellicle. (c and d) SEM images of CA. (e and f) TEM images of CA.

temperature using a three-electrode system consisting of the NiS/CA composite electrode, platinum, and Ag/AgCl electrode as the working electrode, counter electrode, and reference electrode, respectively. The electrochemical properties were evaluated *via* a CHI 660D electrochemical workstation (Chenhua Instruments Co., China). Cyclic voltammetry (CV) curves were obtained at different scan rates in the voltage range of 0–0.5 V, and galvanostatic charge/discharge curves were measured in the voltage range of 0–0.5 V. Electrochemical impedance spectroscopy (EIS) measurements were carried out in the frequency range of 10^5–0.01 Hz at an open circuit potential with the amplitude of 5 mV.

The specific capacitance (C_m) of electrodes can be calculated from CV curves according to the following equation:[6]

$$C_m = \frac{1}{mv\Delta V}\int i(V)\mathrm{d}V \quad (1)$$

where I is the response current (A), V is the potential (V), and ν is the mass of the electroactive materials in the electrodes (g).

The specific capacitance can also be calculated according to the non-linear charge–discharge curves by the following equations:[42]

$$E_{int/D} = I\int_{t(V_{max})}^{t(V_{min})} V(t)\mathrm{d}t \quad (2)$$

$$C_m = \frac{2E_{int/D}}{{V_{max}}^2} \quad (3)$$

where $E_{int/D}$ (Wh kg^{-1}) is the charge energy, I (A) is the applied current, t (s) is the charge time, and V (V) is the charge potential.

Electrochemical measurements of the asymmetric supercapacitors

The asymmetric supercapacitor (ASC) was assembled using NiS/CA-2 composite aerogel and CA as the positive and negative electrode materials, respectively. The mass ratio of the NiS/CA-2 composite to CA was set based on the following equation:[43]

$$\frac{m_+}{m_-} = \frac{C_- \times V_-}{C_+ \times V_+} \quad (4)$$

where C is the specific capacitance (F g^{-1}) obtained from the three-electrode system, V is the potential window (V), and m is the mass of the electrode (g).

The galvanostatic charge–discharge curves of the assembled ASC device were measured at different current densities ranging from 1 to 10 A g^{-1} to evaluate the specific capacitance, energy density, and power density of the ASC device by the following equations:[44]

$$C_m = \frac{I_d \times \Delta t}{\Delta V} \quad (5)$$

$$E = \frac{1}{2} \times C \times V^2 \quad (6)$$

$$P = \frac{E}{\Delta t} \quad (7)$$

where C_m (F g^{-1}), V (V), Δt (s), E (Wh kg^{-1}), P (W kg^{-1}) are the specific capacitance, potential window, discharge time, energy density, and power density, respectively.

Results and discussion

Morphology and characterization of CA and NiS/CA composite aerogels

The main preparation process of sheet-like CAs derived from BC is schematically illustrated in Fig. 1a. The first step was to obtain dried BC pellicle by freeze-drying, which involved the purification of BC pellicle. The following step was the dissolution of the dried BC pellicle to form a homogeneous slurry (step 2 in Fig. 1a). This solution was then heated at 80 °C for a few hours to form a freestanding gel through regeneration (step 3 in Fig. 1a). After being kept in water for several hours and freeze-dried, BC aerogel with good shape integrity was obtained (step 4 in Fig. 1a). The BC aerogel was then subjected to carbonization under a N_2 atmosphere at 800 °C to obtain the CA aerogel (step 5 in Fig. 1a). Finally, NiS particles were successfully anchored on the pore walls of the CA aerogel by a solvothermal process (step 6 in Fig. 1a).

SEM observations indicated that the original BC pellicle has nanofibrous network structures comprising intertwined nanofibers with diameters ranging from several to tens of nanometers (Fig. 1b). However, the morphology of the as-obtained CA aerogel (Fig. 1c and d) is quite different from that of the directly carbonized BC pellicle (c-BC) (Fig. S1, see ESI†). Both the SEM and TEM images (Fig. S1, see ESI†) of c-BC reveal that c-BC maintained the nanofibrous network structures of the original BC pellicle although it had been through a high-temperature carbonization process. However, sheet-like laminar structures rather than fibrous were observed in the SEM image of CA aerogel (Fig. 1c and d). The SEM image reveals that the sheet-like laminas assembled to form a 3D porous structure with pore size ranging from 1 to 30 μm. Furthermore, TEM images (Fig. 1e and f) also depict that sheet-like structure rather than fibrous can be observed in the CA aerogel, indicating that BC pellicle was reconstructed into a new type of architecture by the dissolution and regeneration process. As reported, alkali hydrates, urea hydrates, and free water formed in the pre-cooled NaOH/urea aqueous solution would surround the cellulose molecules, which can penetrate cellulose and destroy the intra- and inter-molecular hydrogen bonds of cellulose, resulting in solvation of the cellulose chains. However, the hydrates in the cellulose aqueous solution are unstable at high temperature. When the cellulose solution was treated at 80 °C, the hydrates surrounding the cellulose chains suffered from decomposition and the intra- and inter-molecular hydrogen bonds in cellulose chains were enhanced. As a result, the cellulose chains re-assembled to sheets due to the hydrogen bond effects. Furthermore, the

surface area and pore size of CA were tested by BET analysis (Fig. S2, see ESI†). As shown in Fig. S2,† although the CA aerogel showed lower pore volume, ascribing to the dissolution–gelation process, CA still exhibited a relatively high surface area (367.5 m^2 g^{-1}) and the mesopores in CA had a ~2 nm average size (Fig. S2b, see ESI†). Benefiting from the sheet-like laminar structures produced during the re-gelation process, CA showed much higher electrical conductivity compared with c-BC (Table S1†), which may accelerate the electron transfer. Therefore, the well-connected channels of CA provided large surface area and highly active regions for the growth of NiS and facilitated the diffusion of electrolyte ions in the pores.[45]

Fig. 2 reveals the typical SEM images of NiS-decorated CA composite aerogels with varied NiS content. As indexed in Fig. 2c and d, benefiting from the sheet-like porous structure of CA, NiS particles with rough surface were uniformly anchored on the pore walls of CA. Moreover, benefiting from this unique structure, the electrode/electrolyte contact area can be effectively improved and the ions diffusion path can be significantly shortened for faster charge transfer reaction at the electrode/electrolyte interface. In addition, with the increase of added precursors of NiS, the amount of irregular NiS particles immobilized on CA framework was increased. However, with the initial nickel salt content increased to 6 mmol, the NiS particles tended to agglomerate, which restricted the permeation of electrolyte into the electrode and further decreased the electrode/electrolyte contact area (Fig. 2e and f). In contrast, neat NiS (Fig. S3a and S3b, see ESI†) shows heavy aggregations of particles and thin sheets, which will severely hinder the electrochemical performance of NiS.

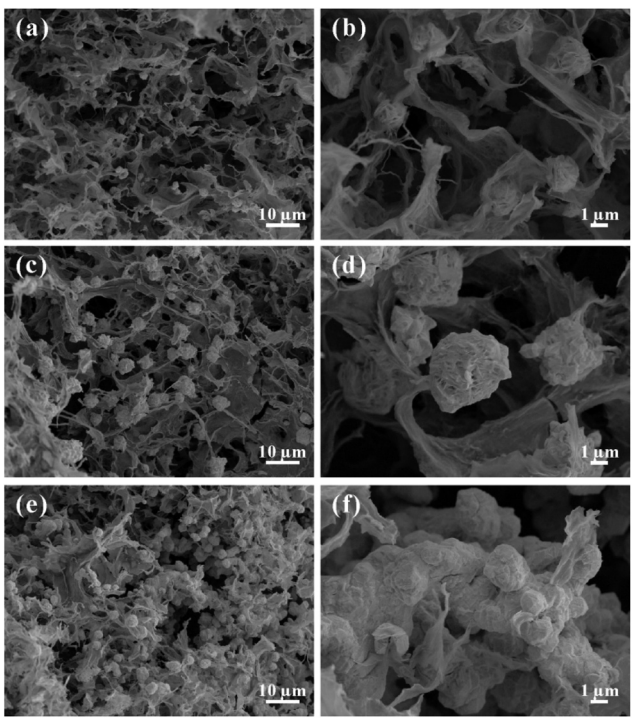

Fig. 2 SEM images of (a and b) NiS/CA-1, (c and d) NiS/CA-2, and (e and f) NiS/CA-3.

The crystal structures of pure NiS, CA, and NiS/CA composite aerogels were investigated by XRD. As revealed in Fig. 3a, the peaks centred at 18.9°, 30.8°, 32.7°, 36.2°, 37.9°, 41.0°, 49.3°, 50.7°, 53.1°, 57.9°, 60.1°, 66.8°, 68.2°, 73.5°, and 76.1° are assigned to (110), (101), (300), (021), (220), (211), (131), (410), (401), (330), (012), (103), (200), (112), and (202) planes of β-NiS, respectively, which are distinctly observed in the XRD patterns of NiS and NiS/CA composites.[46] However, note that for both neat NiS and NiS/CA composites, the peaks appeared at 2θ = 46.1° and 53.9° can be easily indexed to α-NiS (JCPDS card no. 02-1280),[46] indicating the co-existence of α- and β-NiS on the pore walls of CA. Regarding the CA sample, two peaks observed at about 2θ = 26° and 44° can be attributed to the (002) and (100) planes of carbon (JCPDS no. 01-0646), respectively, suggesting that the obtained CA possessed low crystallinity. Therefore, the XRD patterns illustrate that α- and β-form crystal NiS were successfully immobilized on the pore walls of CA.

To further investigate the surface chemical compositions and electronic state of NiS/CA-2 composite aerogels, XPS measurements were performed. As shown in Fig. 3b, the peaks at 163.5, 284.5, and 856.5 eV refer to S 2p, C 1s, and Ni 2p, respectively, whereas that at 532.5 eV refers to O 1s, implying the co-presence of S, C, Ni, and O elements in NiS/CA-2 composite aerogels.[24,47] Two main peaks at 861.5 and 856.3 eV in the Ni 2p high-resolution spectrum (as depicted in Fig. 3c) are assigned to Ni $2p_{3/2}$ and the satellite peak.[23] The high-resolution S 2p spectrum (Fig. 3d) shows two intense peaks at 168.3 and 163.3 eV corresponding to S $2p_{1/2}$ and S $2p_{3/2}$, respectively, suggesting the presence of divalent sulfide ions (S^{2-}) in the NiS/CA-2 sample.[24] Therefore, the XPS spectra also revealed that NiS was successfully grown on CA, which is consistent with the XRD analysis.

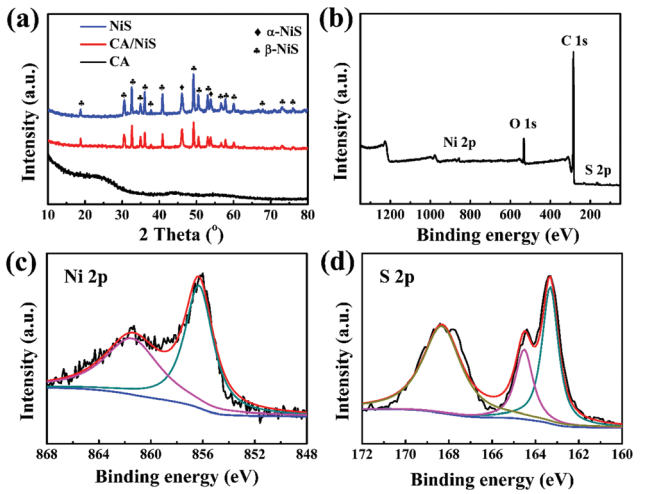

Fig. 3 (a) XRD patterns of pure NiS, CA, and NiS/CA. (b) XPS survey spectrum, (c) Ni 2p high-resolution spectrum, and (d) S 2p high-resolution spectrum of NiS/CA-2.

Raman spectra of CA, pure NiS, and NiS/CA-2 composite are shown in Fig. S4.† Obviously, various Raman peaks of pure NiS can be observed, in which, the peak at ~142 cm^{-1} can be found in both α- and β-form NiS, peaks at ~238 cm^{-1} and ~341 cm^{-1} belong to the vibration of α-form NiS, and the peak at ~300 cm^{-1} can be attributed to β-form NiS.[48,49] Additionally, the Raman spectrum of CA shows two peaks at ~1345 cm^{-1} (D band) and ~1593 cm^{-1} (G band), corresponding to the presence of sp^3 defects and the in-plane vibration of sp^2 carbon atoms, respectively.[50] Compared with pure NiS and CA, all the above mentioned characteristic bands were observed in the NiS/CA composite aerogels, confirming that the NiS/CA composite aerogels were successfully fabricated.

Electrochemical performance of CA and NiS/CA composite aerogels

To explore the electrochemical performance of NiS/CA composite aerogels as electrode materials for supercapacitors, CV curves, galvanostatic charge–discharge curves, and electrochemical impedance (EIS) analysis of the composite aerogels were investigated in 2 M KOH electrolyte. Fig. 4a reveals the typical CV curves of neat NiS and NiS/CA composites obtained at the scan rate of 10 mV s^{-1}. Obvious anodic peak and cathodic peaks in the potential range of 0–0.5 V were observed in the CV curves of all the samples, suggesting the pseudocapacitive characteristics of NiS and their composites. The redox peaks show that the redox reactions were mainly a result of reversible conversions among NiS, NiSOH, and NiSO in alkaline electrolyte, which can be briefly illustrated as follows:[51]

$$NiS + OH^- \underset{\text{Discharge}}{\overset{\text{Charge}}{\longleftrightarrow}} NiSOH + e^- \quad (8)$$

$$NiSOH + OH^- \underset{\text{Discharge}}{\overset{\text{Charge}}{\longleftrightarrow}} NiSO + H_2O + e^- \quad (9)$$

Additionally, it was observed that areas enveloped and current densities for all the NiS/CA composite aerogels were higher than those of neat NiS electrode at the same scan rate, suggesting much higher specific capacitance. The detailed specific capacitances of neat NiS and pure CA, as well as the NiS/CA composites were further calculated from the CV curves at the scan rate of 10 mV s^{-1} according to a reported work[52]

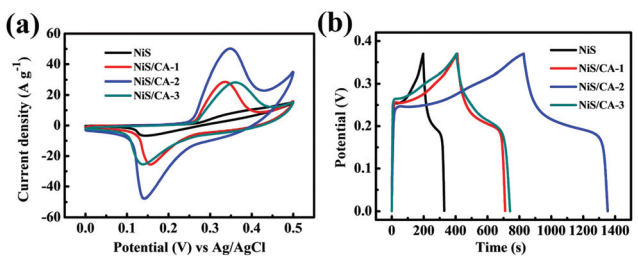

Fig. 4 (a) CV curves of pure NiS and NiS/CA composite aerogels at the scan rate of 10 mV s^{-1} and (b) galvanostatic charge–discharge curves of pure NiS and NiS/CA composite aerogels at the current density of 1 A g^{-1}.

(Fig. S5, see ESI†). Obviously, all the NiS/CA composite aerogels showed much higher capacitance than neat NiS and CA. The enhanced specific capacitance in the composites may be derived from the 3D porous structures of CAs, providing a higher electrical conductivity and preventing the aggregation of NiS nanoparticles, thus offering more redox active sites than the neat NiS. Furthermore, NiS/CA-2 exhibited the maximum area of closed CV curve among the composite electrodes, suggesting the highest specific capacitance, which may be derived from the appropriate ratio between NiS and CA and proper size of NiS. In contrast, for the NiS/CA-1 sample, few NiS particles led to few redox active sites (Fig. 2a and b), and the overabundant NiS grown on CA resulted in apparent aggregations for NiS/CA-3 (Fig. 2e and f).

Fig. 4b depicts the galvanostatic charge–discharge curves of pure NiS and NiS/CA composite aerogels measured at the current density of 1 A g^{-1}. Obviously, the galvanostatic charge–discharge curves of neat NiS and NiS/CA composites exhibited distinct pseudocapacitive behaviour, which is consistent with the CV curves. Note that NiS/CA-2 sample displays a specific capacitance of 1606 F g^{-1} at the current density of 1 A g^{-1}, calculated according to eqn (2) and (3), which is much higher than those of all the other electrodes. The superior supercapacitive performance of the NiS/CA-2 composite electrode can be attributed to the following structural features. First, the unique sheet-like structure of CA could enhance the electron transport during the charge–discharge process owing to its high electrical conductivity. Second, the highly open 3D porous structures provides a short transfer pathway and good accessibility for the electrolyte, supplying a buffering substrate to accommodate the local volumetric expansion/contraction of NiS particles during long-term cycling. For comparison, the electrochemical performance of CA electrode materials prepared by the same method was also investigated. As shown in Fig. S6,† CA electrode showed no pseudocapacitive characteristic in the potential window of 0.0–0.5 V. Moreover, the specific capacitance of CA revealed from the galvanostatic charge–discharge curve exhibited a relatively low value of about 73 F g^{-1} at the current density of 1 A g^{-1}. Therefore, the synergistic effect of NiS and CA had greatly improved the specific capacitance of the composite aerogel electrodes.

To further investigate the electrochemical performance of NiS/CA composite electrode for supercapacitors, the rate capabilities of the NiS/CA-2 at various scan rates were obtained (Fig. 5). It was apparent that along with the scan rate increasing from 5 to 100 mV s^{-1}, both the corresponding current densities and the distance between the anodic and cathodic peaks increased, reflecting that fast electron transfer occurred at the interface of active materials and electrolyte.[23] The capacitance value obtained at the scan rate of 5 mV s^{-1} is ~1368.8 F g^{-1}. Moreover, at the high scan rate of 100 mV s^{-1}, the NiS/CA-2 sample still showed a high capacitance retention of ~312 F g^{-1} (Fig. S7, see ESI†), suggesting good rate stabilities of the NiS/CA composite aerogels.

The rate performance of NiS/CA composite aerogel was further evaluated by the charge–discharge test at various

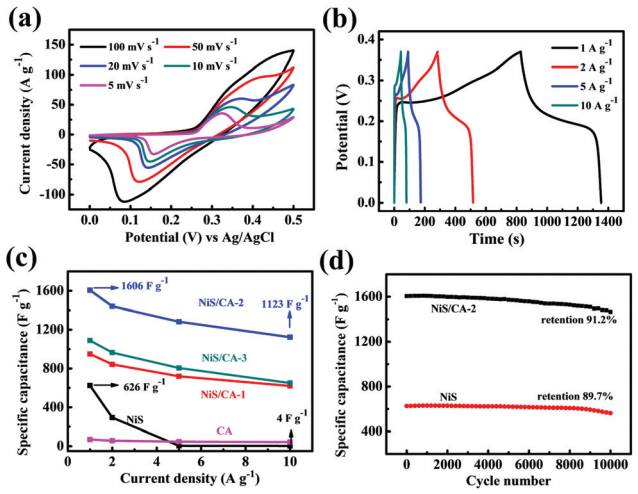

Fig. 5 (a) CV curves of NiS/CA-2 at different scan rates from 5 mV s^{-1} to 100 mV s^{-1}, (b) galvanostatic charge–discharge curves of NiS/CA-2 at different current densities from 1 A g^{-1} to 10 A g^{-1}, (c) specific capacitance plots of NiS, CA, and NiS/CA samples at different current densities, and (d) cycling performance of pure NiS and NiS/CA-2 sample at the scan rate of 100 mV s^{-1} for 10 000 cycles.

current densities, as shown in Fig. 5b. Specific capacitances of the NiS/CA-2 electrode were 1606, 1440, 1283, and 1123 F g^{-1} at the current densities of 1, 2, 5, and 10 A g^{-1}, respectively. With the increase of current density from 1 to 10 A g^{-1}, 69.9% capacitance was retained for NiS/CA-2, whereas only 1% capacitance was retained for pure NiS (Fig. 5c), indicating much better rate performance of the NiS/CA-2 electrode. To the best of our knowledge, the specific capacitance value of NiS/CA-2 is comparable or even higher than previous reported values (Table 1). The enhanced specific capacitance of NiS/CA may be attributed to the synergistic effect between the abundant active sites offered by CA and the relative high theoretical capacitance of NiS, as well as the well-defined open porous structures of CA, which allows for facile access of electrolyte to the active materials and facilitates the charge transport and ion diffusion between active materials and conductive substrate. Therefore, NiS/CA is a type of potential electrode materials for high performance supercapacitors.

The cycling performance of NiS/CA-2 was also investigated to further evaluate the potential of NiS/CA-2 composite as electrode materials for supercapacitors. As depicted in Fig. 5d, cycling test for NiS/CA-2 as well as neat NiS were performed by sweeping the CV curves in the potential range of 0–0.5 V at the scan rate of 100 mV s^{-1} for 10 000 cycles. Obviously, the NiS/CA-2 composite as an electrode material displayed good cycling stability with a stable capacitance (retention 91.2%) after 10 000 CV cycles. Note that at the initial 1000 cycles for NiS/CA-2 and NiS, the specific capacitances increased as a result of increased available active sites due to the electrode activation effect.

EIS measurements were performed to further investigate the properties of conductivity and charge transport behaviour of the NiS/CA composites. As shown in Fig. 6, the Nyquist plots for both the NiS and NiS/CA composite electrodes comprise a semicircle in the high-frequency region and a straight line in the low-frequency region, which are related to the charge transfer resistance and ion diffusion resistance in the electrode, respectively.[58] The NiS/CA-2 sample exhibited a much smaller radius in the high-frequency region compared with the NiS electrode, indicating its lower faradaic charge transfer resistance. The NiS/CA-2 electrode exhibited a more vertical line than the NiS electrode in the low-frequency region, illustrating better capacitive behaviour and lower diffusion resistance of ions. Moreover, close observation from Fig. 6b shows that the NiS/CA-2 has a much smaller intersection of the curves at the real axis than NiS, indicating much smaller equivalent series resistance. Note that due to the low charge transfer resistance of the CA electrode, the Nyquist plot did not exhibit a semicircle in the high-frequency region. These EIS results confirm that the NiS/CA-2 composite pos-

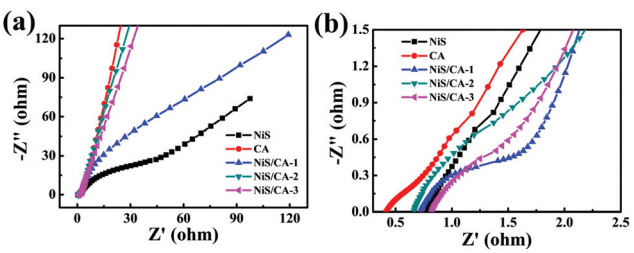

Fig. 6 (a) Nyquist plots of NiS, CA, and NiS/CA composite electrodes measured in the frequency range from 100 kHz to 0.01 Hz and (b) enlargement of the Nyquist plots in the high frequency region.

Table 1 Comparison between NiS-based composites for supercapacitors

Electrodes based on materials	Maximum C_s (F g^{-1})	C_s (F g^{-1}) or capacity retention (%) after several cycles	Ref.
NiS/graphene-covered make-up cotton	775 (0.5 A g^{-1})	557 (2 A g^{-1}, 1000 cycles)	23
α-NiS	1092 (1 A g^{-1})	~100% (5 mV s^{-1}, 2000 cycles)	46
NiS/graphene	1420 (2 A g^{-1})	994 (6 A g^{-1}, 2000 cycles)	50
Nickel cobalt sulfide ball-in-ball hollow spheres	1036 (1.0 A g^{-1})	750 (5 A g^{-1}, 2000 cycles)	53
Flower-like NiS	1318 (5 mV s^{-1})	778 (4 A g^{-1}, 3000 cycles)	54
Flower-like β-NiS	1606 (2 A g^{-1})	44.2% (2 A g^{-1}, 1000 cycles)	55
NiS hollow spheres	927 (4 A g^{-1})	587 (4.2 A g^{-1}, 1000 cycles)	56
Porous NiS nanoflakes arrays	718 (2 A g^{-1})	82.6% (2 A g^{-1}, 3000 cycles)	57
NiS/CA	1606 (1 A g^{-1})	1465 (1 A g^{-1}, 10 000 cycles)	This work

sessed a scaffold that could allow for the efficient diffusion of electrolyte to the surface of electrode and accelerate the electron transport, contributing to significant improvement in the electrochemical performance.

Electrochemical performance of the asymmetric supercapacitors

An asymmetric supercapacitor (ASC) was assembled utilizing NiS/CA-2 composite and CA as the positive and negative electrode materials, respectively, according to previously reported work,[44,52] which was assigned as NiS/CA-2//CA. The advantage of the ASC configuration is the use of a pseudocapacitive electrode as a positive electrode to enhance the specific capacitance of the cell. On the other hand, the working potential of the ASC device could also be extended owing to the overpotential of the reversible hydrogen electrosorption in the carbon-based negative electrode.[59] First, the CV measurements at various voltage windows were used to evaluate the operating potential of the ASC device (Fig. S8, see ESI†). In the CV curves, there is an obvious bump and sharp increase at 1.6 V, which may be due to some type of irreversible reactions, indicating instability of the device at the operating potentials over 1.4 V. The specific capacitance calculated by CV curves increased from 14.9 to 50.4 F g^{-1} as the potential window was increased from 0.8 to 1.4 V (Fig. S9, see ESI†). As a result, the overall performance of the ASC device could be remarkably improved. Operating at higher voltage usually reduced the number of devices in series required to reach the desired output voltage for practical applications.[60] Therefore, an operating voltage window of 1.4 V was chosen to further study the superior electrochemical performance of the as-obtained ASC device.

The CV curves of the ASC device at the scan rates of 5–200 mV s^{-1} are shown in Fig. 7a. The redox peaks can be clearly identified in the CV curves, indicating the pseudocapacitive behaviour of the device because of the faradaic reaction of NiS. With the increasing scan rate, the faradaic reactions became more intense. The CV shape was well maintained even at a high scan rate of 200 mV s^{-1}, revealing the fast charge–discharge properties of the ASC device. The effect of scan rate on the specific capacitance was also investigated by calculating the specific capacitance derived from the CV curves. As depicted in Fig. S10,† with the increased scan rate, the specific capacitance gradually decreased from 90.5 F g^{-1} at the scan rate of 5 mV s^{-1} to 40.7 F g^{-1} at a high scan rate of 200 mV s^{-1}, which can be attributed to inefficient utilization of the electroactive materials at a high scan rate.[61]

The galvanostatic charge–discharge measurements performed at various current densities of 1–10 A g^{-1} are shown in Fig. 7b. It is clear that all the discharge curves show pseudocapacitve behaviour. The specific capacitance values calculated by eqn (5) are estimated to be 79.1, 64.9, 60.4, 55.4, and 47.9 F g^{-1} at the current densities of 1, 2, 3, 5, and 10 A g^{-1}, respectively (Fig. 7c). At a high current density of 10 A g^{-1}, the ASC device still exhibited a high capacitance retention of 60.6%, which is attributed to the synergistic effect between the 3D porous structure constructed by CA and high capacitance of NiS particles. This clearly indicated that this asymmetric device can provide more reliable capacitive performance at high rates for high power applications.

Moreover, Nyquist plots of the ACS device were acquired to further investigate its electrochemical behaviour with rapid electron-transfer and diffusion process during the charge–discharge reaction (Fig. 7d). The typical Nyquist plot includes two

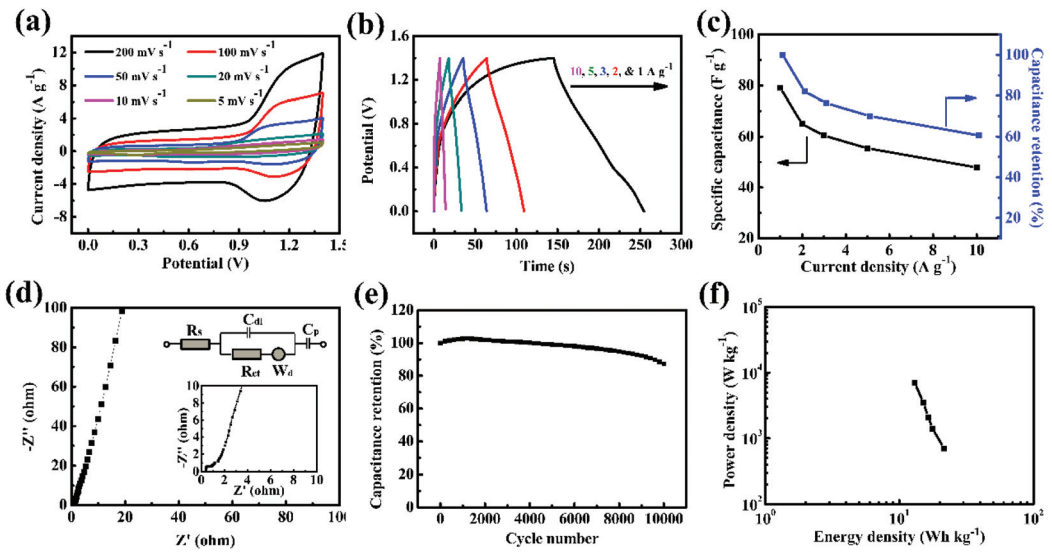

Fig. 7 (a) CV curves at various scan rates ranging from 5 mV s^{-1} to 200 mV s^{-1}, (b) galvanostatic charge–discharge curves at different current densities, (c) specific capacitance and the corresponding capacitance retention, (d) Nyquist plots, high frequency region and an equivalent circuit for fabricated ASC device, (e) the long-term cycling performance at the scan rate of 100 mV s^{-1} of the assembled NiS/CA-2//CA device, and (f) Ragone plot related to energy and power densities operated at different operating voltages.

regions: one is the high-frequency region (see inset), which comprises a small semicircle indicating low resistance at the electrode/electrolyte interface and the other is the low-frequency region, in which the impedance plot is almost parallel to the vertical axis indicating the excellent capacitive behaviour of the supercapacitor.[62] The equivalent series resistance including bulk electrolyte resistance, contact resistances, and bulk electrode resistance, as estimated from the *x*-intercept of the Nyquist plot, was found to be ~0.39 Ω. Furthermore, an equivalent circuit for the Nyquist plot is also given in the inset, where R_s and R_{ct} are the series and charge transfer resistances, respectively, W_d is the Warburg resistance, and C_{dl} and C_p are the double layer and pseudocapacitor capacitance values, respectively. Moreover, the obtained EIS data were further analysed using Bode plots, which represent the change in the phase angle with respect to applied frequency. As shown in Fig. S11,† the phase angle is about −81° at 0.01 Hz, which is close to that of an ideal capacitor (−90°),[63] indicating that the assembled NiS/CA-2//CA device possesses good capacitive behaviour.

Furthermore, the long-term cycling stability of the ASC device was also evaluated (Fig. 7e). After 10 000 cycles, the device still maintained a high capacitance retention of ~87.1%. The increase of specific capacitances at the beginning is probably due to the activation effect that allows the trapped ions to gradually diffuse outward. Additionally, the cycling performance of ASC device was also investigated at the high current density of 10 A g^{-1}. As shown in Fig. S12,† after 10 000 cycles, ~86% capacitance retention was maintained, demonstrating the as-prepared device has high cycling performance even at the high current density of 10 A g^{-1}. To further determine the cycling stability of the assembled device, the voltage-holding (floating) tests of the assembled device were performed (see the ESI† for details). Fig. S13(a)† shows the voltage-holding curve for the period of 120 h, which shows a slight decrease in the capacitance retention. Up to the end of the floating test, the assembled device still exhibited high capacitance retention up to 90%, signifying that the device possesses excellent stability and no significant degradation. Fig. S13(b)† displays the resistance as a function of the floating time; it can be seen that the resistance showed a slight increase during floating at 1.4 V, indicating almost no aging of the assembled device at this voltage.

To evaluate the energy storage performance of the ASC device, the energy and power densities were calculated based on eqn (6) and (7) and plotted on the Ragone diagram (Fig. 7f). The maximum energy density for the ASC device operating at the voltage window of 1.4 V is ~21.5 Wh kg^{-1} at the power density of 700 W kg^{-1}. As the current density increased, the energy density slightly decreased and the power density increased. Even at the high current density of 10 A g^{-1}, the energy density was 13.0 Wh kg^{-1} and power density was 7 kW kg^{-1}. Therefore, the as-obtained ASC device shows very good power density without much loss in energy density, which can be attributed to the synergistic effect of CA and NiS. The excellent performance of the ASC device can be explained by the following reasons. On the one hand, CA with 3D porous structure, high surface area, and good electric conductivity provides abundant active sites for effective growth of NiS particles, electrochemical reaction, short ion-diffusion path, and fast charge-transfer speed during charge–discharge. On the other hand, NiS particles anchored on pore walls of CA enhance the capacitance and rate performance. Therefore, the as-obtained NiS/CA-2 composite aerogel is a promising alternative in high-performance electrode materials for supercapacitors.

Conclusions

In summary, sheet-like carbon aerogels were prepared from BC pellicles by employing a dissolution–gelation–carbonization approach, which was used as a framework to construct NiS/CA composite aerogels with NiS uniformly decorated on the pore walls of CA. The NiS/CA composite electrodes exhibited excellent specific capacitance (1606 F g^{-1} at 1 A g^{-1}), good rate capacitance retention (69% at 10 A g^{-1}), and improved cycling stability (92.1% retention after 10 000 continuous CV cycles). The as-assembled ASC device obtained using NiS/CA composite and CA as the positive and negative electrode materials, respectively, has a wide operating voltage window of 1.4 V. The ASC device also exhibits a high specific energy of ~21.5 Wh kg^{-1} at the power density of 700 W kg^{-1} and excellent capacitive retention of ~87.1% after 10 000 cycles of CV scans. Therefore, an effective combination of electroactive materials with high theoretical capacities and carbon aerogels with highly porous structures can produce high-performance electrode materials for asymmetric supercapacitors. Furthermore, our study offers a new strategy to fabricate 3D porous carbon materials derived from the low-cost cellulose-based materials (*e.g.* waste paper, plant cellulose, lignin, *etc.*), which may have great potential applications in energy storage devices.

Acknowledgements

We are really grateful for the financial support received from the National Natural Science Foundation of China (51433001, 21674019), the Initial Research Funds for Young Teachers of Donghua University, the Program of Shanghai Academic Research Leader (17XD1400100), and the Saint-Gobain Research (Shanghai) Co., Ltd.

Notes and references

1 Y. H. Li, L. J. Cao, L. Qiao, M. Zhou, Y. Yang, P. Xiao and Y. H. Zhang, *J. Mater. Chem. A*, 2014, **2**, 6540–6548.
2 W. Fan, C. Zhang, W. W. Tjiu, K. P. Pramoda, C. B. He and T. X. Liu, *ACS Appl. Mater. Interfaces*, 2013, **5**, 3382–3391.
3 Y. E. Miao, W. Fan, D. Chen and T. X. Liu, *ACS Appl. Mater. Interfaces*, 2013, **5**, 4423–4428.

4 M. K. Liu, W. W. Tjiu, J. S. Pan, C. Zhang, W. Gao and T. X. Liu, *Nanoscale*, 2014, **6**, 4233–4242.
5 L. L. Zhang and X. S. Zhao, *Chem. Soc. Rev.*, 2009, **38**, 2520–2531.
6 L. S. Zhang, Q. W. Ding, Y. P. Huang, H. H. Gu, Y. E. Miao and T. X. Liu, *ACS Appl. Mater. Interfaces*, 2015, **7**, 22669–22677.
7 C. D. Lokhande, D. P. Dubal and O. S. Joo, *Curr. Appl. Phys.*, 2011, **11**, 255–270.
8 F. L. Lai, Y. E. Miao, Y. P. Huang, T. S. Chung and T. X. Liu, *J. Phys. Chem. C*, 2015, **119**, 13442–13450.
9 W. T. Deng, X. B. Ji, Q. Y. Chen and C. E. Banks, *RSC Adv.*, 2011, **1**, 1171–1178.
10 W. Fan, Y. E. Miao, L. S. Zhang, Y. P. Huang and T. X. Liu, *RSC Adv.*, 2015, **5**, 31064–31073.
11 E. Frackowiak and F. Beguin, *Carbon*, 2001, **39**, 937–950.
12 W. Fan, Y. E. Miao, Y. P. Huang, W. W. Tjiu and T. X. Liu, *RSC Adv.*, 2015, **5**, 9228–9236.
13 G. A. Snook, P. Kao and A. S. Best, *J. Power Sources*, 2011, **196**, 1–12.
14 L. F. Shen, J. Wang, G. Y. Xu, H. S. Li, H. Dou and X. G. Zhang, *Adv. Energy Mater.*, 2015, **5**, 14009773.
15 Y. Gao, L. W. Mi, W. T. Wei, S. Z. Cui, Z. Zheng, H. W. Hou and W. H. Chen, *ACS Appl. Mater. Interfaces*, 2015, **7**, 4311–4319.
16 L. F. Shen, L. Yu, H. B. Wu, X. Y. Yu, X. G. Zhang and X. W. Lou, *Nat. Commun.*, 2015, **6**, 6694–6701.
17 W. J. Zhou, X. J. Wu, X. H. Cao, X. Huang, C. L. Tan, J. Tian, H. Liu, J. Y. Wang and H. Zhang, *Energy Environ. Sci.*, 2013, **6**, 2921–2924.
18 T. Zhu, B. Xia, L. Zhou and X. W. D. Lou, *J. Mater. Chem.*, 2012, **22**, 7851–7855.
19 L. H. Zhuo, Y. Q. Wu, L. Y. Wang, Y. C. Yu, X. B. Zhang and F. Y. Zhao, *RSC Adv.*, 2012, **2**, 5084–5087.
20 L. Zhang, H. B. Wu and X. W. D. Lou, *Chem. Commun.*, 2012, **48**, 6912–6914.
21 S. J. Bao, C. M. Li, C. X. Guo and Y. Qiao, *J. Power Sources*, 2008, **180**, 676–681.
22 L. S. Zhang, Y. P. Huang, Y. F. Zhang, H. H. Gu, W. Fan and T. X. Liu, *Adv. Mater. Interfaces*, 2016, **3**, 1500467.
23 Y. J. Li, K. Ye, K. Cheng, J. L. Yin, D. X. Cao and G. L. Wang, *J. Power Sources*, 2015, **274**, 943–950.
24 Z. M. Zhang, Q. Wang, C. J. Zhao, S. D. Min and X. Z. Qian, *ACS Appl. Mater. Interfaces*, 2015, **7**, 4861–4868.
25 Y. F. Zhang, W. Fan, Y. P. Huang, C. Zhang and T. X. Liu, *RSC Adv.*, 2015, 1301–1308.
26 H. Y. Sun, Z. Xu and C. Gao, *Adv. Mater.*, 2013, **25**, 2554–2560.
27 T. J. Kang, T. Kim, E. Y. Jang, H. Im, X. Lepro-Chavez, R. Ovalle-Robles, J. Oh, M. E. Kozlov, R. H. Baughman, H. H. Lee and Y. H. Kim, *Sci. Rep.*, 2014, **4**, 6105–6109.
28 C. H. Wang, X. D. He, Y. Y. Shang, Q. Y. Peng, Y. Y. Qin, E. Z. Shi, Y. B. Yang, S. T. Wu, W. J. Xu, S. Y. Du, A. Y. Cao and Y. B. Li, *J. Mater. Chem. A*, 2014, **2**, 14994–15000.
29 W. Gao, Y. E. Miao, C. Zhang, Z. Yang, Z. Y. Liu, W. W. Tjiu and T. X. Liu, *ACS Appl. Mater. Interfaces*, 2013, **5**, 7584–7591.
30 Y. Q. Li, Y. A. Samad, K. Polychronopoulou, S. M. Alhassan and K. Liao, *ACS Sustainable Chem. Eng.*, 2014, **2**, 1492–1497.
31 W. S. Chen, Q. Li, Y. C. Wang, X. Yi, J. Zeng, H. P. Yu, Y. X. Liu and J. Li, *ChemSusChem*, 2014, **7**, 154–161.
32 H. L. Cai, S. Sharma, W. Y. Liu, W. Mu, W. Liu, X. D. Zhang and Y. L. Deng, *Biomacromolecules*, 2014, **15**, 2540–2547.
33 H. Hu, Z. B. Zhao, W. B. Wan, Y. Gogotsi and J. S. Qiu, *Adv. Mater.*, 2013, **25**, 2219–2223.
34 X. T. Zhang, Z. Y. Sui, B. Xu, S. F. Yue, Y. J. Luo, W. C. Zhan and B. Liu, *J. Mater. Chem.*, 2011, **21**, 6494–6497.
35 Y. Zhou, S. L. Candelaria, Q. Liu, Y. X. Huang, E. Uchaker and G. Z. Cao, *J. Mater. Chem. A*, 2014, **2**, 8472–8482.
36 H. Jin, H. M. Zhang, H. X. Zhong and J. L. Zhang, *Energy Environ. Sci.*, 2011, **4**, 3389–3394.
37 X. Z. Xu, J. Zhou, D. H. Nagaraju, L. Jiang, V. R. Marinov, G. Lubineau, H. N. Alshareef and M. Oh, *Adv. Funct. Mater.*, 2015, **25**, 3193–3202.
38 C. T. Chen, Y. Huang, C. L. Zhu, Y. Nie, J. Z. Yang and D. P. Sun, *Chin. J. Polym. Sci.*, 2014, **32**, 439–448.
39 C. L. Long, D. P. Qi, T. Wei, J. Yan, L. L. Jiang and Z. J. Fan, *Adv. Funct. Mater.*, 2014, **24**, 3953–3961.
40 S. H. Li, D. K. Huang, B. Y. Zhang, X. B. Xu, M. K. Wang, G. Yang and Y. Shen, *Adv. Energy Mater.*, 2014, **4**, 1301655.
41 F. L. Lai, Y. E. Miao, Y. P. Huang, Y. F. Zhang and T. X. Liu, *ACS Appl. Mater. Interfaces*, 2016, **8**, 3558–3566.
42 A. Laheaeaer, P. Przygocki, Q. Abbas and F. Beguin, *Electrochem. Commun.*, 2015, **60**, 21–25.
43 J. Cai, H. T. Niu, Z. Y. Li, Y. Du, P. Cizek, Z. L. Xie, H. G. Xiong and T. Lin, *ACS Appl. Mater. Interfaces*, 2015, **7**, 14946–14953.
44 F. Lai, Y. Miao, L. Zuo, H. Lu, Y. Huang and T. Liu, *Small*, 2016, **12**, 3235–3244.
45 P. Hao, Z. Zhao, J. Tian, H. Li, Y. Sang, G. Yu, H. Cai, H. Liu, C. P. Wong and A. Umar, *Nanoscale*, 2014, **6**, 12120–12129.
46 C. C. Sun, M. Z. Ma, J. Yang, Y. F. Zhang, P. Chen, W. Huang and X. C. Dong, *Sci. Rep.*, 2014, **4**, 7054–7059.
47 W. T. Wei, L. W. Mi, Y. Gao, Z. Zheng, W. H. Chen and X. X. Guan, *Chem. Mater.*, 2014, **26**, 3418–3426.
48 D. W. Bishop, P. S. Thomas and A. S. Ray, *Mater. Res. Bull.*, 1998, **33**, 1303–1306.
49 D. W. Bishop, P. S. Thomas and A. S. Ray, *Mater. Res. Bull.*, 2000, **35**, 1123–1128.
50 Z. Zhang, X. J. Liu, X. Qi, Z. Y. Huang, L. Ren and J. X. Zhong, *RSC Adv.*, 2014, **4**, 37278–37283.
51 F. Cai, R. Sun, Y. R. Kang, H. Y. Chen, M. H. Chen and Q. W. Li, *RSC Adv.*, 2015, **5**, 23073–23079.
52 R. R. Salunkhe, J. J. Lin, V. Malgras, S. X. Dou, J. H. Kim and Y. Yamauchi, *Nano Energy*, 2015, **11**, 211–218.
53 Z. M. Zhang, C. J. Zhao, S. D. Min and X. Z. Qian, *Electrochim. Acta*, 2014, **144**, 100–110.
54 J. Q. Yang, W. Guo, D. Li, C. Y. Wei, H. M. Fan, L. Y. Wu and W. J. Zheng, *J. Power Sources*, 2014, **268**, 113–120.

55 J. Q. Yang, X. C. Duan, Q. Qin and W. J. Zheng, *J. Mater. Chem. A*, 2013, **1**, 7880–7884.
56 T. Zhu, Z. Y. Wang, S. J. Ding, J. S. Chen and X. W. Lou, *RSC Adv.*, 2011, **1**, 397–400.
57 X. Y. Yan, X. L. Tong, L. Ma, Y. M. Tian, Y. S. Cai, C. W. Gong, M. G. Zhang and L. P. Liang, *Mater. Lett.*, 2014, **124**, 133–136.
58 J. Li, H. Q. Xie, Y. Li, J. Liu and Z. X. Li, *J. Power Sources*, 2011, **196**, 10775–10781.
59 V. Khomenko, E. Raymundo-Pinero and F. Beguin, *J. Power Sources*, 2006, **153**, 183–190.
60 A. Izadi-Najafabadi, S. Yasuda, K. Kobashi, T. Yamada, D. N. Futaba, H. Hatori, M. Yumura, S. Iijima and K. Hata, *Adv. Mater.*, 2010, **22**, 235–241.
61 Z. J. Lao, K. Konstantinov, Y. Tournaire, S. H. Ng, G. X. Wang and H. K. Liu, *J. Power Sources*, 2006, **162**, 1451–1454.
62 A. Singh, A. J. Roberts, R. C. T. Slade and A. Chandra, *J. Mater. Chem. A*, 2014, **2**, 16723–16730.
63 L. Y. Yuan, X. Lu, X. Xiao, T. Zhai, J. J. Dai, F. C. Zhang, B. Hu, X. Wang, L. Gong, J. Chen, C. G. Hu, Y. X. Tong, J. Zhou and Z. L. Wang, *ACS Nano*, 2012, **6**, 656–661.